AIAA JOURNAL
Vol. 32, No. 12, December 1994

Effect of Grid Aspect Ratio on Convergence

P. E. O. Buelow,* S. Venkateswaran,† and Charles L. Merkle‡
Pennsylvania State University, University Park, Pennsylvania 16802

The effects of high-aspect-ratio grids on algorithm convergence are considered by means of vector stability theory and computational experiments. The results indicate that approximately factored implicit schemes experience convergence deterioration because of nonoptimum local time-stepping procedures and increased need for viscous preconditioning. Based on this insight, an enhanced algorithm is devised using improved selection of the local time step, appropriate definition of the viscous preconditioning matrix, and proper implementation of the boundary conditions. The new algorithm provides uniformly efficient convergence at all aspect ratios for both Euler and Navier-Stokes computations for a variety of test problems.

Introduction

MULTIDIMENSIONAL Navier-Stokes codes are routinely used for flowfield computations in a variety of applications. For simple flowfields with simple geometries, these algorithms generally converge efficiently, are robust, and pose no problem to the user. As the complexity of the flowfield increases, however, the robustness and convergence efficiency generally begin to disappear, and increased user intervention is required to obtain a final solution.

Several contributing phenomena lead to this degradation in overall robustness. Code performance may be compromised by the lack of proper grid resolution, inappropriate initial conditions, or because the flowfield lies outside the regime in which the algorithm converges efficiently. An example of the latter effect is the presence of extended low-Mach-number regions where the disparity between the acoustic and particle speeds causes convergence deterioration in time-marching methods. Recent research into this problem by several workers including the present authors has largely negated this difficulty through the introduction of time-derivative preconditioning.[1-6] The related problem at low Reynolds numbers, where the disparity between wave propagation and viscous damping rates slows the convergence, has likewise been addressed through preconditioning.[2,3,6]

In the present paper, we consider still another factor that can play a crucial role in the convergence of Navier-Stokes computations—namely, sensitivity to grid stretching and high grid aspect ratios. This situation is particularly characteristic of turbulent flow calculations where the grid near the wall must be refined to resolve the steep velocity gradient. In such instances, high-aspect-ratio grids cause disparity in the wave propagation speeds (or, more precisely, in the time scales) in the two coordinate directions, causing serious convergence deterioration. The purpose of the present paper is to identify the specific reasons for this convergence degradation and to demonstrate methods for providing uniform convergence for all grid aspect ratios.

Several researchers have examined grid aspect ratio effects as part of studies on algorithm performance[7-9] but not as an end in itself. The present paper represents the first study in which aspect ratio effects are the main focus. The approach that we follow is first to systematically examine the performance of numerical algorithms as a function of grid aspect ratio and then to devise enhanced algorithmic procedures to improve convergence in flowfields with high-aspect-ratio regions. We focus our attention in this paper on centrally differenced schemes to gain fundamental understanding that can later be extended to other schemes. Furthermore, for these initial studies, we concentrate primarily on the alternating direction implicit (ADI) algorithm,[10-12] although, for perspective, we discuss explicit schemes briefly.

We start by presenting the preconditioned Navier-Stokes equations[3] that, as mentioned earlier, provide excellent convergence over the entire Mach number and Reynolds number domains for regular-sized grid cells. We then use vector stability analyses to examine the characteristics of the ADI algorithm for the Euler and Navier-Stokes equations using grid aspect ratio as a parameter. These stability results raise several issues that must be addressed in high-aspect-ratio computations. These include 1) the precise definition of local time step, which is straightforward for regular-sized grids but must be done very carefully at high aspect ratios, 2) the correct choice of viscous preconditioning, which is especially important in highly stretched grids because small cell Reynolds numbers are encountered even in high-Reynolds-number flows, and 3) the proper implementation of boundary conditions. In general, the application of each of these issues separately has little impact, but when applied in combination, they provide very efficient convergence at all grid aspect ratios.

To test the performance of the enhanced algorithm in the presence of high-aspect-ratio grids, we consider a variety of problems in the section entitled Results. The test cases include inviscid and viscous flow in a straight duct (with aspect ratios ranging from unity to one million), laminar and turbulent boundary layers, multispecies shear layers at various Reynolds numbers, and turbulent heat flux computations in a converging-diverging nozzle with cooled walls. Results from these computations demonstrate convergence rates that are virtually independent of grid aspect ratio, thereby providing convergence speedups of up to two orders of magnitude over conventional algorithms.

Preconditioned Navier-Stokes Algorithm

Preconditioned Navier-Stokes Equations

The preconditioned Navier-Stokes equations are given by

$$\Gamma\frac{\partial Q_v}{\partial t}+\frac{\partial E}{\partial x}+\frac{\partial F}{\partial y}=H+L(Q_v) \tag{1}$$

Here, the flux vectors E and F have their traditional definitions for the equations in conservative form,

$$E=\begin{bmatrix}\rho u\\(\rho u^2+p)\\\rho uv\\(e+p)u\end{bmatrix},\qquad F=\begin{bmatrix}\rho v\\\rho uv\\(\rho v^2+p)\\(e+p)v\end{bmatrix}$$

but, for convenience, the traditional primary dependent variable is replaced by the vector

$$Q_v=(p,u,v,T)^T$$

Received June 28, 1993; revision received March 14, 1994; accepted for publication March 15, 1994.

*Graduate Research Assistant, Propulsion Engineering Research Center, Department of Mechanical Engineering.

†Research Associate, Propulsion Engineering Research Center, Department of Mechanical Engineering.

‡Distinguished Alumni Professor, Propulsion Engineering Research Center, Department of Mechanical Engineering.

The diffusive terms are also in their standard conservative form,[3]

$$L = \frac{\partial}{\partial x} R_{xx} \frac{\partial}{\partial x} + \frac{\partial}{\partial x} R_{xy} \frac{\partial}{\partial y} + \frac{\partial}{\partial y} R_{yx} \frac{\partial}{\partial x} + \frac{\partial}{\partial y} R_{yy} \frac{\partial}{\partial y}$$

Finally, H is the vector containing axisymmetric source terms.

A preconditioning matrix Γ that insures uniform convergence at all Reynolds and Mach number regions is[3]

$$\Gamma = \begin{bmatrix} 1/\epsilon c^2 & 0 & 0 & 0 \\ u/\epsilon c^2 & \rho & 0 & 0 \\ v/\epsilon c^2 & 0 & \rho & 0 \\ \dfrac{h + \frac{1}{2}(u^2+v^2)}{\epsilon c^2} - 1 & \rho u & \rho v & \rho C_p \end{bmatrix} \tag{2}$$

The parameter ϵ in this matrix is responsible for activating the inviscid and viscous preconditioning of the system. Its functional value depends on the local Mach number and Reynolds number as

$$\epsilon = \max(\epsilon_{\text{inv}}, \epsilon_{\text{vis}}) \tag{3}$$

where the subscripts inv and vis refer to inviscid and viscous, respectively.

At locations where the cell Reynolds numbers are high, inviscid preconditioning is activated ($\epsilon = \epsilon_{\text{inv}}$). This inviscid preconditioning parameter is chosen to insure that the acoustic speed and the fluid velocity are the same order of magnitude at all flow Mach numbers. This insures well-conditioned eigenvalues. One effective choice[3] is to set ϵ_{inv} equal to the square of the local Mach number for subsonic flow and to unity for supersonic flow.

At locations where the cell Reynolds numbers are low, viscous preconditioning is activated ($\epsilon = \epsilon_{\text{vis}}$). This preconditioning simultaneously optimizes the relevant inviscid time step (i.e., CFL_{u+c}) and the viscous time step (the von Neumann number VNN given by $\nu\Delta t/\Delta x^2$ or $\nu\Delta t/\Delta y^2$). In previous work,[2,3] CFL_x and VNN_x were maintained at the prescribed value when the grid aspect ratio ($AR = \Delta x/\Delta y$) was less than unity, whereas CFL_y and VNN_y were fixed when AR was greater than unity. Based on these two situations, ϵ_{vis} depends on the two parameters $\alpha = CFL/(VNN \cdot Re_{\Delta x})$ and $\beta = CFL/(VNN \cdot Re_{\Delta y})$ where $Re_{\Delta x}$ and $Re_{\Delta y}$ are the cell Reynolds numbers in the respective coordinate directions and CFL and VNN are the prescribed values of these time scales:

$$\epsilon_{\text{vis}} = \max\left[\frac{\alpha(\alpha-1)}{(\alpha - 1 + c^2/u^2)}, \frac{\beta(\beta-1)}{(\beta - 1 + c^2/v^2)} \right] \tag{4}$$

This procedure is ineffective at high-aspect ratios, and a modification is presented later.

Application of the ADI Algorithm

The numerical solution of Eq. (1) is obtained by using Euler implicit temporal discretization and second-order central differencing for the spatial discretizations. The resulting matrix operator may be approximately factored for efficient inversion.[10–12] When expressed in delta form, this becomes

$$\left(S + \frac{\partial A}{\partial x} - \frac{\partial}{\partial x} R_{xx} \frac{\partial}{\partial x}\right) S^{-1} \left(S + \frac{\partial B}{\partial y} - \frac{\partial}{\partial y} R_{yy} \frac{\partial}{\partial y}\right) \times \Delta Q_v = -\mathcal{R}^n \tag{5}$$

where the residual $\mathcal{R}^n$ is the steady-state version of Eq. (1), and the remaining terms are defined as

$$S = \frac{\Gamma}{\Delta t} - D, \qquad A = \frac{\partial E}{\partial Q_v}, \qquad B = \frac{\partial F}{\partial Q_v}, \qquad D = \frac{\partial H}{\partial Q_v}$$

Time-Step Definition and the Problem at High-Aspect Ratios

Researchers in computational fluid dynamics (CFD) invariably use local time stepping to specify a different physical time step (Δt) at every grid point. This is generally done by setting the dominant or maximum CFL at any grid location to a specified "optimum" number. Mathematically, this max-CFL definition is obtained by computing the minimum time step in the two directions,

$$\Delta t = \min\left(\frac{CFL\Delta x}{\lambda_x}, \frac{CFL\Delta y}{\lambda_y} \right) \tag{6}$$

Here, λ_x and λ_y are the acoustic eigenvalues in the respective coordinate directions. The CFL number is typically taken to be between 1 and 10 for optimum convergence. (The preconditioning matrix insures that the other inviscid and viscous time scales are automatically optimized by the earlier choice of optimum Δt.)

The time step definition in Eq. (6) illustrates the problem experienced with high-aspect-ratio grids. When the aspect ratio is much greater than unity, the $CFL_{\max}$ (CFL_y in this case) is maintained at the optimum value, whereas CFL_x is very small (i.e., $CFL_y = CFL$ and $CFL_x \approx CFL/AR$, assuming that λ_x and λ_y are of the same order). This disparity results in very slow propagation of waves in the streamwise direction, causing poor convergence. The converse situation exists for aspect ratios that are much less than unity. Here, $CFL_x = CFL$ and $CFL_y \approx AR \cdot CFL$, and errors propagate very slowly in the cross-stream direction. These effects are examined in detail in the following sections.

Analysis of High-Aspect-Ratio Convergence

To develop an understanding of the manner in which high-aspect-ratio grids affect convergence and the methods for alleviating these factors, we start from stability analyses of the governing equations in vector form. To illuminate the separate contributions of the convective and diffusive terms, we first consider the Euler equations and treat the convective terms alone. We then turn to the complete Navier-Stokes equations where both convective and diffusive effects are present.

Euler Equation Analysis

The inviscid version of Eq. (1) (the preconditioned Euler equations) is obtained by dropping the diffusive operator. The stability characteristics of this Euler system based on the ADI approximate factorization scheme are given in Figs. 1–3. In these figures (as well as in the other stability results in this paper), contours of the maximum eigenvalue of the amplification matrix are plotted in (k_x, k_y) wave number space. Figure 1 shows the results for two values of CFL, 1 and 10, for grid aspect ratio unity. To conserve space, we take advantage of symmetry and show both results on one plot. For $CFL = 1$ (the left half of Fig. 1), the amplification factor indicates

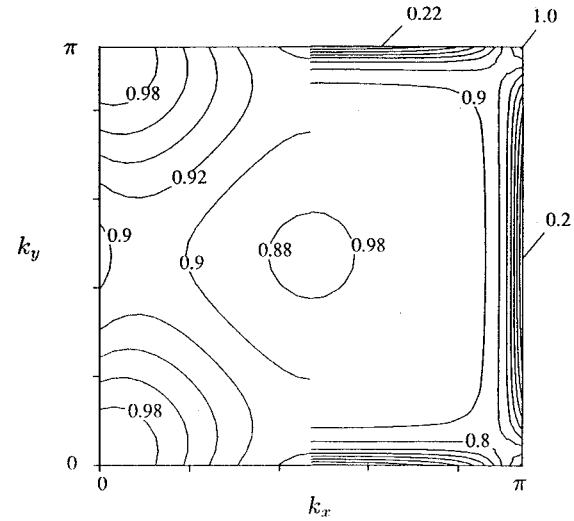

Fig. 1 Euler stability (AR = 1): CFL = 1 (left side); CFL = 10 (right side).

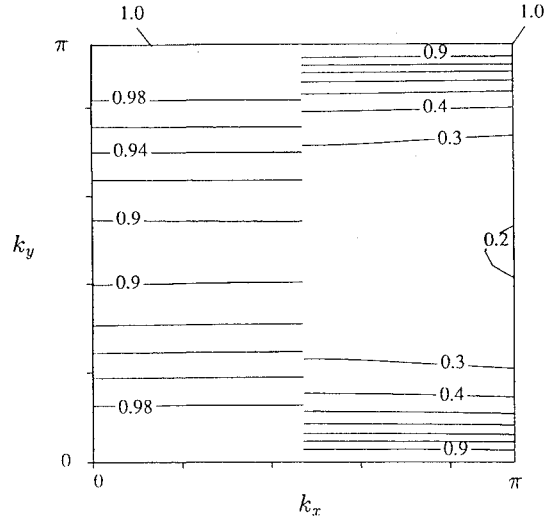

Fig. 2 Euler stability (AR = 100): CFL_x = 0.01 and CFL_y = 1 (left side); CFL_x = 0.1 and CFL_y = 10 (right side).

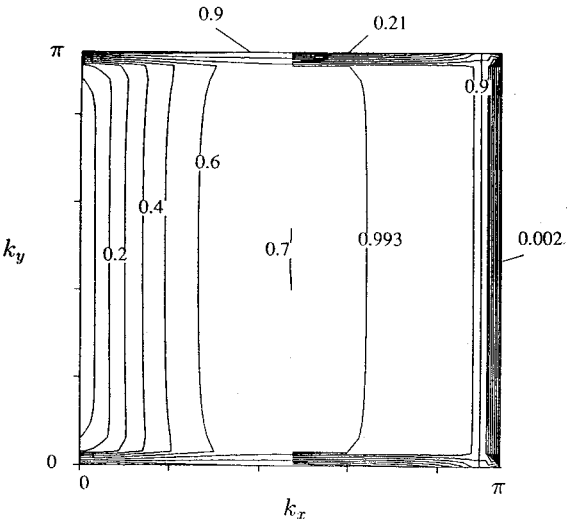

Fig. 3 Euler stability (AR = 100): CFL_x = 1 and CFL_y = 100 (left side); CFL_x = 10 and CFL_y = 1000 (right side).

good damping over the whole wave number domain, whereas for $CFL = 10$ (the right half of Fig. 1), the approximate factorization error causes the amplification factor to approach unity over much of the domain. These results thus demonstrate the well-known ADI result that the optimum CFL lies between 1 and 10.

At $AR = 100$, the results are considerably different as Figs. 2 and 3 show. Here, we must now distinguish between CFL_x and CFL_y. Figure 2 shows stability results for $CFL_x = 0.01$ and $CFL_y = 1$ on the left half, and $CFL_x = 0.1$ and $CFL_y = 10$ on the right half. From the traditional max-CFL time-step definition in Eq. (6), these correspond to specified $CFL_{\max}$ values of 1 and 10, respectively. For both of these cases, the amplification factor approaches unity along the abscissa of the stability diagram. These results imply that the scheme possesses fairly good damping of cross-stream disturbances but very poor damping of longitudinal (or streamwise) disturbances, a consequence of the low CFL_x values. Numerical experiments with a preconditioned Euler code confirm that convergence at these values of CFL is seriously affected for high-grid-aspect ratios, and the residual errors suggest that the longitudinal modes are the controlling factor. It is interesting that, at the higher CFL condition (right half) in Fig. 2, the effect of approximate factorization is not evident as it is in Fig. 1.

Stability results for $CFL_{\max} = 100$ and 1000 are shown in Fig. 3. (Here, $CFL_x = 1$ and $CFL_y = 100$ on the left half, and $CFL_x = 10$ and $CFL_y = 1000$ on the right half.) Despite the high $CFL_{\max}$ value, the amplification factors on the left still show little evidence of the approximate factorization error. The amplification factor not only is, in fact, well conditioned over the midwave numbers but also is now well conditioned for purely longitudinal waves. This latter result is a consequence of the fact that CFL_x is unity. In the right half of Fig. 3, the effect of approximate factorization finally becomes evident, and the amplification factor approaches unity over most of the wave number domain. Thus, for an aspect ratio of 100, the optimum $CFL_{\max}$ (i.e., CFL_y) lies between 100 and 1000. The corresponding optimum CFL_x lies between 1 and 10.

The results in Figs. 2 and 3 (and numerous other results not shown) suggest that the optimum $CFL_{\max}$ for the ADI scheme scales as the aspect ratio, whereas the minimum CFL remains at a fixed value (between 1 and 10). Thus, if the optimum $CFL_{\max}$ is 5 for an aspect ratio of unity, then for $AR = 100$, it would be 500, and for $AR = 1 \times 10^6$, the optimum $CFL_{\max}$ would be 5×10^6. For all of these cases, the optimum time-step size may be obtained by choosing the minimum CFL (i.e., CFL_x) to be 5. In particular, this surprising result indicates that, if the local time step is chosen carefully, the ADI scheme will not suffer convergence deterioration at any grid aspect ratio.

Summarizing these results, we conclude that the constant value of CFL that should be used for all aspect ratios is the one based on the minimum of CFL_x and CFL_y, not the maximum. Mathematically, this new time-step definition may be enforced by selecting the maximum Δt in the two directions rather than the minimum [as in Eq. (6)]:

$$\Delta t = \max\left(\frac{CFL\Delta x}{\lambda_x}, \frac{CFL\Delta y}{\lambda_y}\right) \tag{7}$$

We will henceforth refer to this definition as the min-CFL time step in contrast to the standard max-CFL definition in Eq. (6). Note that the min-CFL definition automatically accounts for both longitudinally and transversely stretched grids.

In the results section, we will see that, when applied by itself, the min-CFL time-step definition suggested by stability theory is not sufficient to insure efficient convergence at all aspect ratios. In fact, this alternative gives little improvement unless it is used in conjunction with properly implemented boundary conditions. We discuss the correct boundary procedures in a later section, but first we extend these Euler stability findings to the Navier-Stokes equations where high-aspect-ratio grids are most prevalent.

Navier-Stokes Analysis

An important aspect of high-aspect-ratio Navier-Stokes computations is the significance of viscous preconditioning. High-aspect-ratio problems are generally dominated by viscous processes in one coordinate direction (this is why highly stretched grids are employed), even when the streamwise Reynolds number is high. The purpose of viscous preconditioning is to optimize the inviscid and viscous modes of the problem simultaneously. For regular-sized grids, the maximum inviscid and viscous time scales are optimized by the viscous preconditioning parameter given in Eq. (4). For high-aspect-ratio grids, the question of which scales must be optimized is not as clear, especially in light of the previous findings for the inviscid equations. In this section, we consider the definition of the viscous preconditioning parameter for high-aspect-ratio situations.

Both scalar and vector analyses of the inviscid equations indicate that the optimum CFL number may be obtained for all grid aspect ratios by fixing the minimum CFL rather than the maximum. A similar analysis of a scalar diffusion equation shows that the optimum VNN is likewise properly determined by the minimum VNN. Furthermore, for a combined scalar convection-diffusion equation, the optimum time step may be determined by choosing the most restrictive amongst the min-CFL and min-VNN time steps. Unfortunately, this simple redefinition of the time step does not carry over directly to the Navier-Stokes equations.

Stability results for the full Navier-Stokes equations are given in Fig. 4 for $AR = 1000$ using this min-CFL, min-VNN definition. Results for $CFL_x = 1$ and $VNN_x = 1$ are shown on the left half, and for $CFL_x = 10$ and $VNN_x = 10$ on the right half. The results on the left half ($CFL_x = 1$, $VNN_x = 1$, $CFL_y = 1000$, and $VNN_y = 1 \times 10^6$) show good damping over most of the wave number domain except for a stiff region at the top of the domain

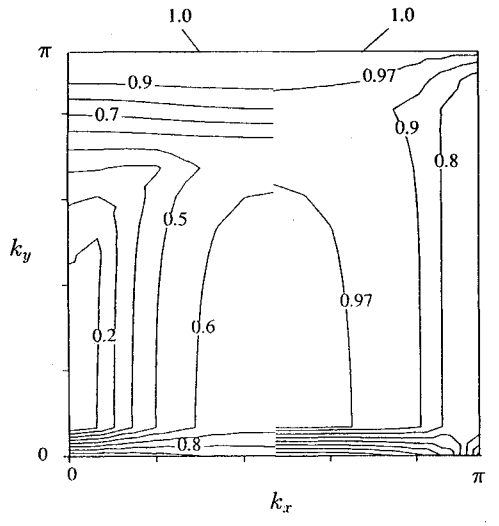

Fig. 4 Navier-Stokes stability (AR = 1000): CFL_x = 1 and VNN_x = 1 (left side); CFL_x = 10 and VNN_x = 10 (right side).

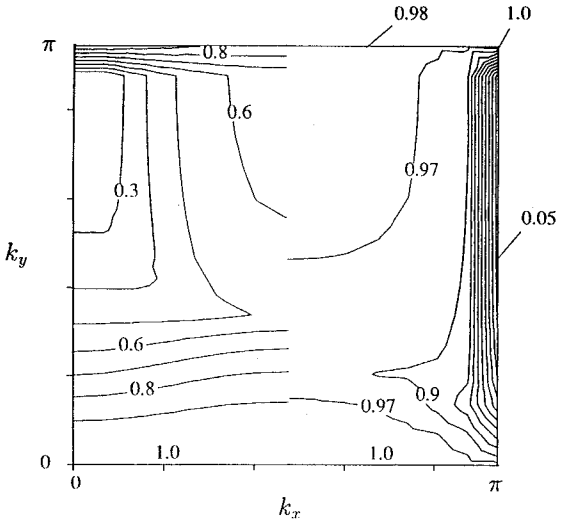

Fig. 5 Navier-Stokes stability (AR = 1000): CFL_x = 1 and VNN_y = 1 (left side); CFL_x = 10 and VNN_y = 10 (right side).

around the $(\pi/2, \pi)$ point where the amplification factor approaches unity. Careful examination reveals that the source of this stiffness is the approximate factorization error from the cross product of the streamwise inviscid term and the cross-stream viscous term. The magnitude of this error term is loosely given by the product of CFL_x and VNN_y. Because VNN_y is large, this error term dominates the other terms in the equation. Exact analysis is difficult for the vector system, but this indicates that scalar results do not always carry over to the vector system.

Experiments with a preconditioned Navier-Stokes code for high-aspect-ratio problems likewise indicate that the min-CFL, min-VNN time-step definition does not perform well. In fact, the convergence rates obtained are quite poor, which suggests that the stiffness in the amplification factor is the controlling factor.

Since the problem associated with the min-CFL, min-VNN definition arises from the approximate factorization product of CFL_x and VNN_y, the error term can be minimized by reducing VNN_y. This may be achieved by specifying the maximum VNN rather than the minimum, while continuing to specify the minimum CFL number. Such a definition, which we refer to as min-CFL, max-VNN, retains the benefits of the min-CFL definition for the "inviscid" modes of the problem while maintaining the conventional restriction on the maximum allowable VNN for the "viscous" modes. Thus, for aspect ratios greater than unity, ϵ_{vis} is chosen to maintain CFL_x and VNN_y at the specified optimum values, whereas for aspect ratios less than unity, ϵ_{vis} is chosen to maintain CFL_y and VNN_x. Mathematically, ϵ_{vis} then depends on two new parameters, $\gamma = (CFL \cdot AR)/(VNN \cdot Re_{\Delta y})$ and $\delta = CFL/(VNN \cdot AR \cdot Re_{\Delta x})$, and is given by

$$\epsilon_{\text{vis}} = \max\left[\frac{\gamma(\gamma-1)}{(\gamma-1+c^2/u^2)}, \frac{\delta(\delta-1)}{(\delta-1+c^2/v^2)}\right] \tag{8}$$

Here, the first choice is selected for $AR > 1$, whereas the second one is selected for $AR < 1$. The time-step size is still based on the min-CFL definition given in Eq. (7).

Stability results for the Navier-Stokes equations using this new min-CFL, max-VNN definition are shown in Fig. 5 for AR = 1000. On the left half, $CFL_x = 1$ and $VNN_y = 1$ ($CFL_y = 1000$, $VNN_x = 1 \times 10^{-6}$), whereas on the right half, $CFL_x = 10$ and $VNN_y = 10$ ($CFL_y = 1 \times 10^4$, $VNN_x = 1 \times 10^{-5}$). The amplification factor for the lower CFL and VNN (left half) is seen to be well conditioned except for the region along the abscissa where it approaches unity. The stiffness in this region is caused by the small viscous time step in the streamwise direction and not the approximate factorization error. Although this represents a potential problem for high-aspect-ratio Navier-Stokes computations, our numerical experiments (shown later) indicate that in all cases efficient convergence is obtained using this min-CFL, max-VNN time step.

Application of Boundary Conditions

Conventional Navier-Stokes codes use a wide variety of boundary condition procedures including extrapolation, reflection, and method of characteristics (MOC) procedures. Past experience has indicated that all of these methods work equally well when moderate values of CFL are used. Calculations with direct inversion (no approximate factorization), however, show that MOC procedures are preferred at higher CFL's. Our present analyses of high-aspect-ratio convergence indicate that the $CFL_{\max}$ should scale as the aspect ratio and, hence, will be quite large. This suggests that the boundary procedure can have a significant impact on convergence at high-aspect ratios. In particular, the proper implementation of MOC boundary conditions becomes imperative under such situations.

For approximate factorization schemes, the MOC boundary conditions may be implemented in two ways: 1) after operator factorization[13,14] (which we will refer to as MOC I)

$$\left[\frac{\partial \Omega}{\partial Q_v} + L_s M^{-1}\left(\Gamma + \Delta t \frac{\partial A}{\partial x}\right)\right]$$

$$\times \Gamma^{-1}\left(\Gamma + \Delta t \frac{\partial B}{\partial y}\right)\Delta Q_v = -\Delta t L_s M^{-1}\mathcal{R}^n$$

or 2) before operator factorization (MOC II)

$$\left(S + \Delta t L_s M^{-1}\frac{\partial A}{\partial x}\right)S^{-1}\left(S + \Delta t L_s M^{-1}\frac{\partial B}{\partial y}\right)\Delta Q_v$$

$$= -\Delta t L_s M^{-1}\mathcal{R}^n$$

In these expressions,

$$S = \frac{\partial \Omega}{\partial Q_v} + L_s M^{-1}\Gamma$$

where Ω is the boundary condition vector, M^{-1} is the matrix of left eigenvectors, and L_s is a selection matrix that chooses the appropriate characteristic equations at a given boundary.

We note that MOC II is more correct but MOC I is easier to implement and has been more commonly employed. In the results section, we show that for regular-sized grids both methods work equally well, but for high-aspect-ratio grids, MOC II gives more reliable convergence behavior.

Explicit Schemes

We digress briefly to discuss time-step selection for explicit algorithms. For this purpose, we consider multistage Runge-Kutta methods, which, for the Euler equations, take the form

$$Q_v^k = Q_v^n + \alpha_k \Delta t \Gamma^{-1}\mathcal{R}^{k-1} \qquad k = 1, 2, \ldots, N$$

where N is the number of steps and $\mathcal{R}$ again denotes the residual. The amplification matrix for this equation is given by

$$G = I + \alpha_N \Delta t Z + \alpha_N \alpha_{N-1} \Delta t^2 Z^2 + \cdots + \alpha_N \alpha_{N-1} \cdots \alpha_2 \alpha_1 \Delta t^N Z^N$$

where Z is the Fourier transform of $\mathcal{R}$. Unlike approximately factored implicit systems, this amplification matrix can be easily diagonalized[15] for the Euler equations. This readily leads to the conclusion that the optimum local time step is given by computing the limiting CFL from the sum of the various directional CFL's. Nearly all researchers currently make this time-step choice. Unfortunately, both stability analyses and convergence results show that even with this optimum choice of local time stepping, convergence of Runge-Kutta schemes deteriorates rapidly as aspect ratio is increased. The combination of preconditioning, boundary condition implementation, and time-step selection thus provides no improvements in Runge-Kutta systems.

Results

Analysis of algorithm performance for high-aspect-ratio computations has indicated that the time-step definition, viscous preconditioning, and boundary condition implementation are controlling factors. For efficient convergence at all aspect ratios, the local time step must be selected based on the min-CFL definition, and the viscous preconditioning matrix must be based on optimizing the maximum VNN simultaneously with the minimum CFL. Furthermore, convergence results point to the importance of proper method of characteristics boundary procedures to insure reliable convergence at all aspect ratios.

In this section, we consider various test cases—both simple and complex—to demonstrate the performance of the enhanced algorithmic procedures in the presence of high-grid-aspect-ratio regions in the flowfield. First we consider the simple case of inviscid and viscous flow in a straight duct, which allows us to study grid aspect ratio effects parametrically. Then we look at more realistic problems such as multispecies shear layers, high-Reynolds-number laminar and turbulent boundary layers, and turbulent flow through a choked nozzle with cooled walls. All of these examples involve local regions where the grid is strongly stretched, giving rise to a wide distribution of grid aspect ratios in the flowfield.

Inviscid Flow in Straight Duct

We start by considering the seemingly trivial problem of the solution of the Euler equations for uniform flow in a straight duct. By varying the aspect ratio of the duct while maintaining a fixed grid size (41 x 41), we change the local grid aspect ratio from unity to 1000. The initial condition used for all calculations is uniform flow plus a 1% random error at each grid point. Figure 6 shows the number of iterations required to reach machine accuracy for these computations as a function of the grid aspect ratio. Clearly, it is not necessary to drive convergence to machine error (typically 10^{-16}) for engineering solutions, but it is very useful for diagnosis of algorithm performance.

The convergence results in Fig. 6 are shown for the standard algorithm (with max-CFL time step and MOC I boundary conditions), the enhanced algorithm (with min-CFL time step and MOC II boundary conditions), as well as an intermediate algorithm (with min-CFL time step but MOC I boundary conditions). All three algorithms give nearly identical convergence for aspect ratio unity (about 500 iterations). As aspect ratio is increased, the convergence of the standard algorithm deteriorates seriously. For $AR = 100$, it requires nearly 20,000 iterations. This degradation arises because the longitudinal disturbances are poorly damped, as can be verified by examining the residual errors in the computation. This behavior is in agreement with the predictions of stability theory.

The results for the intermediate algorithm also show no improvement in the overall convergence for aspect ratios of 10 and 100, even though the time step is selected to insure optimum convergence. Inspection of the individual convergence rates for this case shows that the min-CFL time step accelerates convergence dramatically at first, but that after converging several orders of magnitude, the convergence rate changes slope abruptly and flattens considerably. Examination of the residual errors at this stage indicates that

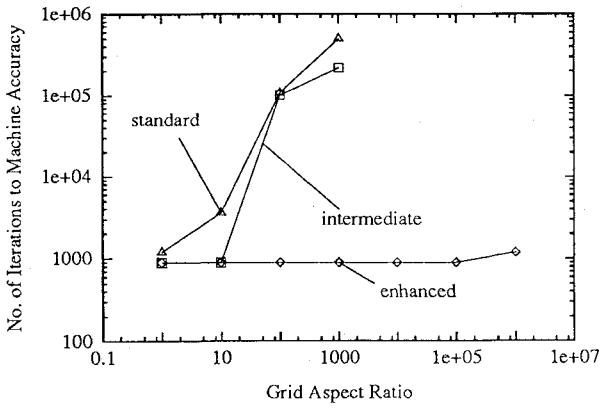

Fig. 6 Convergence for inviscid duct with the aspect ratio as a parameter. Standard = MOC I, max-*CFL*; intermediate = MOC I, min-*CFL*; enhanced = MOC II, min-*CFL*.

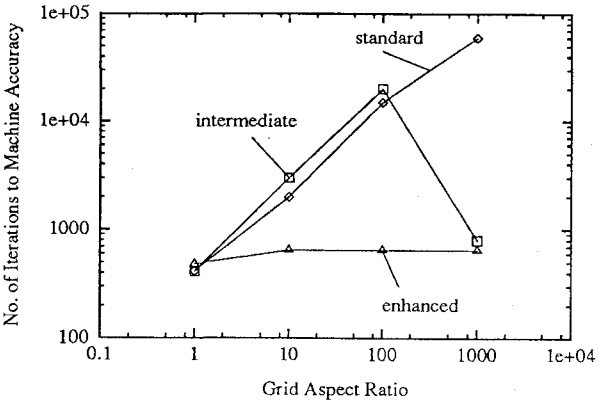

Fig. 7 Convergence for viscous duct with the aspect ratio as a parameter (Re_{Δ_x} = 100). Standard = max-*CFL*, max-*VNN*; intermediate = min-CFL; no viscous preconditioning; enhanced = min-*CFL*, max-*VNN*.

the flattening of convergence is caused by accumulation of errors at the inlet and exit boundaries of the system. This suggests that the treatment of boundary conditions (MOC I) is responsible for the behavior. Interestingly, for $AR = 1000$ and higher, the convergence flattening no longer occurs and convergence is attained in about 1000 iterations. Thus, the impact of boundary conditions on convergence is inconsistent; nevertheless, it is evidence that the improved time step helps convergence but that boundary condition implementation can also be critical.

In contrast, the results for the enhanced algorithm, where the time step is properly defined and the boundary conditions are correctly applied, show very good convergence for all aspect ratios. Convergence is attained in about 600 iterations in each instance. The associated savings in CPU time improve with aspect ratio, reaching nearly two orders of magnitude at $AR = 1000$.

Viscous Flow in Straight Duct

We next present results of a similar parametric study for the solution of the Navier-Stokes equations in Fig. 7. Again, we consider flow in a straight duct and vary the grid aspect ratio by changing the aspect ratio of the flow domain. The grid size is fixed at 41 x 41. We consider aspect ratios ranging from unity to one million. Aspect ratios of one million are often encountered locally in Navier-Stokes computations of turbulent flow. We consider an example of such a flowfield later. The velocity profile at the inlet is taken to be parabolic, obviating the need for grid stretching near the wall. The Mach number of the flow is 1×10^{-5}, and the streamwise cell Reynolds number $Re_{\Delta x}$ is 100. The cross-stream cell Reynolds number $Re_{\Delta y}$ ranges from 100 to 10^{-4} depending on the grid aspect ratio.

Convergence results in Fig. 7 are shown for the standard algorithm (based on max-CFL, max-VNN), the enhanced algorithm (based on min-CFL, max-VNN), and an intermediate algorithm (min-CFL time step but no viscous preconditioning). For all three algorithms, the boundary conditions are enforced using the MOC

II procedure, which the inviscid results indicated as superior. At aspect ratio unity, as in the inviscid case, all three algorithms give excellent convergence behavior, and convergence to machine zero is attained in less than 1000 iterations. At high-aspect ratios, however, the convergence results are dramatically different.

The convergence of the standard algorithm is seen to deteriorate rapidly as aspect ratio is increased. At $AR = 1000$, almost 500,000 iterations are necessary for convergence, indicating a slowdown of a factor of 500. For higher aspect ratios, the slowdown is even greater, and complete convergence cannot be attained within reasonable amounts of computer time.

In contrast, the convergence results for the enhanced algorithm show uniformly good convergence (about 1000 iterations) for all aspect ratios. The enhanced algorithm can dramatically influence the capability of computing flowfields involving very high aspect ratios.

The results for the intermediate algorithm show the importance of viscous preconditioning for high-aspect-ratio Navier-Stokes computations. Note that for all cases $Re_{\Delta x} = 100$, whereas $Re_{\Delta y} = 100$ for $AR = 1$ but is proportionately lower for higher aspect ratios. It is seen that viscous preconditioning becomes important when $AR \geq 100$ because the corresponding $Re_{\Delta y}$ becomes of order 1 or less. Under such conditions, the benefits derived by the min-CFL time step are completely negated by the dominant viscous modes of the problem, and convergence is no better than that for the standard algorithm. These results again highlight the fact that the various controlling issues must be addressed in combination to control the convergence behavior effectively at all aspect ratios.

Multispecies Shear Layer

Having established the performance of the enhanced algorithm for simple cases, we now turn to more realistic flowfields. The first case we examine is a multispecies, nonreacting shear layer. The shear layer consists of coflowing streams of hydrogen and oxygen. The Mach number of both streams is 0.1, and the grid size is 61×61. Grid stretching is employed at the interface between the two streams to resolve the shear layer. The solutions for three different Reynolds numbers (2×10^2, 2×10^3, and 2×10^4 based on the width of the oxygen stream) are shown in Fig. 8. The corresponding maximum grid aspect ratios were 30, 60, and 100, respectively. The hydrogen profiles in Fig. 8 at a given axial location of the flowfield show the extent of species diffusion for the three Reynolds numbers.

The convergence histories for the shear layer are shown in Fig. 9. For the enhanced algorithm (min-CFL, max-VNN, and MOC II boundary conditions), the convergence for all three cases is seen to be very good, reaching machine zero in about 1200 iterations. In particular, the different grid aspect ratios (shown in parenthesis) for the three cases have no effect on the convergence rate.

The other convergence curves shown in Fig. 9 are for the $Re = 2 \times 10^2$ case with one or more aspects of the enhanced algorithm turned off. Curve II is for the standard preconditioned algorithm (max-CFL, max-VNN). The corresponding convergence is about a factor of 3 slower even though the maximum grid aspect ratio for this case is only 30. Thus, even for this simple case, the savings in CPU time can be quite substantial. The remaining convergence plots in Fig. 9 are obtained with the min-CFL time-step definition but without viscous preconditioning (curve III) and without any preconditioning (curve IV). These results once again demonstrate the importance of doing "everything" right to obtain convergence that is independent of grid aspect ratio.

Flat Plate Boundary Layers

As a further Navier-Stokes example, we consider both laminar and turbulent flat plate boundary-layer flowfields. Because of the steep velocity gradients near the wall, strong grid stretching is required at high Reynolds numbers. This wall stretching gives rise to high-aspect-ratio grids adjacent to the wall, whereas the grids away from the wall are more or less a regular size. Convergence results using the enhanced algorithm are given in Fig. 10 for four different Reynolds numbers using grids with correspondingly different extents of wall grid stretching. The three lower Reynolds numbers (4×10^3, 4×10^4, and 4×10^5) are laminar computations, and the corresponding maximum grid aspect ratios (located adjacent to the wall) are 10, 30, and 200. The highest Reynolds number (4×10^6) is a turbulent computation, and the maximum grid aspect ratio for this case is 8000 (y^+ is less than 1). In all cases, the flow Mach number is 0.1, and the grid size is 61×61. For the turbulent boundary-layer computation, the algebraic Baldwin-Lomax turbulence model[16] is employed.

The convergence in Fig. 10 using the enhanced algorithm is extremely good for all four Reynolds numbers. Despite the different aspect ratios of the grid cells for each of the cases, the convergence rates are almost identical, reaching machine zero in about 800 iterations. For comparison, the convergences of one of the laminar cases ($Re = 4 \times 10^5$) and of the turbulent case ($Re = 4 \times 10^6$) using the standard algorithm (max-CFL, max-VNN) are also shown in Fig. 10. For the laminar case, the residuals drop just over an order of magnitude for every 1000 iterations, requiring about 15,000 iterations to reach machine zero. The corresponding convergence speedup of the enhanced algorithm is a factor of about 20. We noted earlier (in Figs. 6 and 7) that the CPU savings typically increase as the grid is further refined. The turbulent computation in Fig. 10 likewise reflects this, and the associated convergence speedup is about 100 times.

The velocity profiles obtained for the $Re = 4 \times 10^5$ laminar calculation and the $Re = 4 \times 10^6$ turbulent calculation are shown in Figs. 11 and 12. The laminar solution (Fig. 11) is compared with

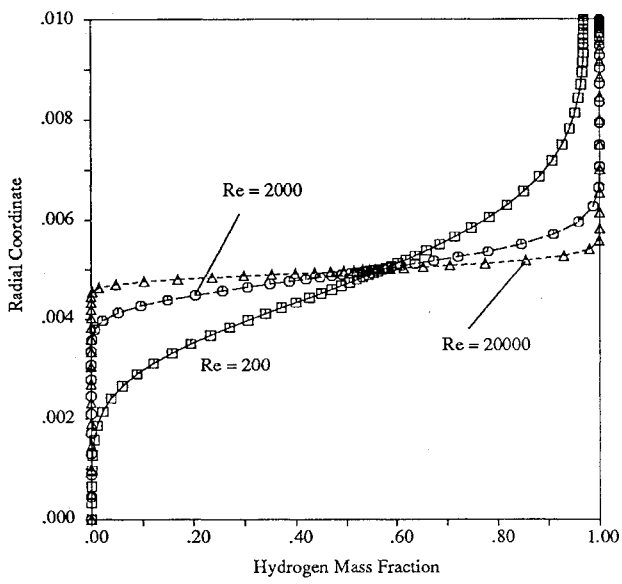

Fig. 8 Shear layer hydrogen mass fraction profiles.

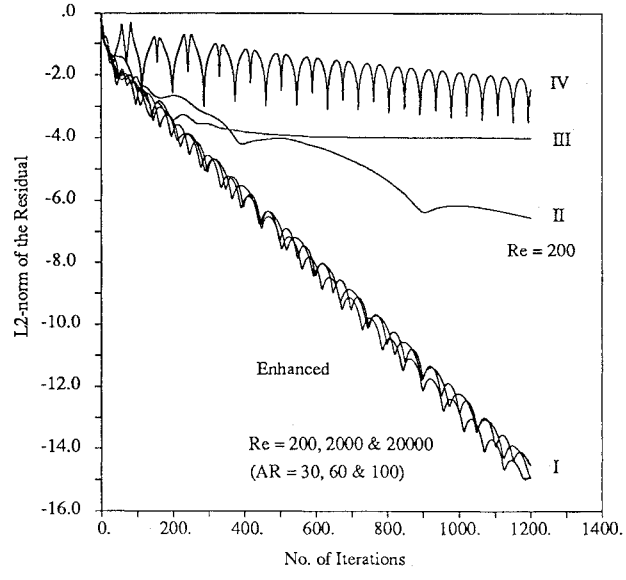

Fig. 9 Convergence for multispecies shear layer for standard and enhanced algorithms.

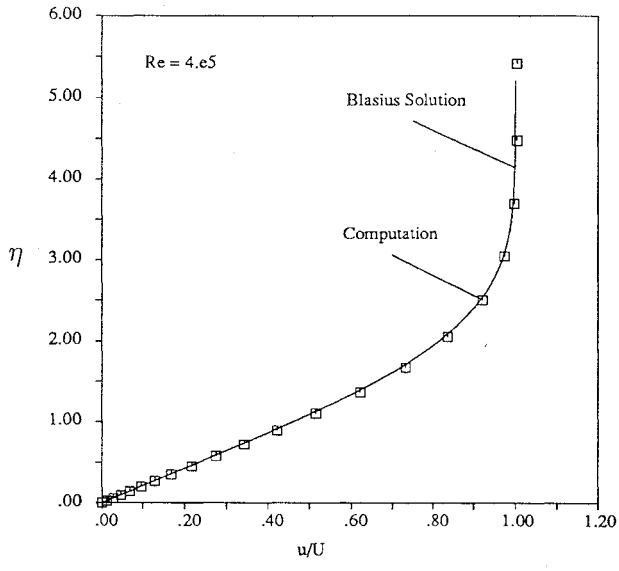

Fig. 10 Convergence for flat plate boundary layer for standard and enhanced algorithms.

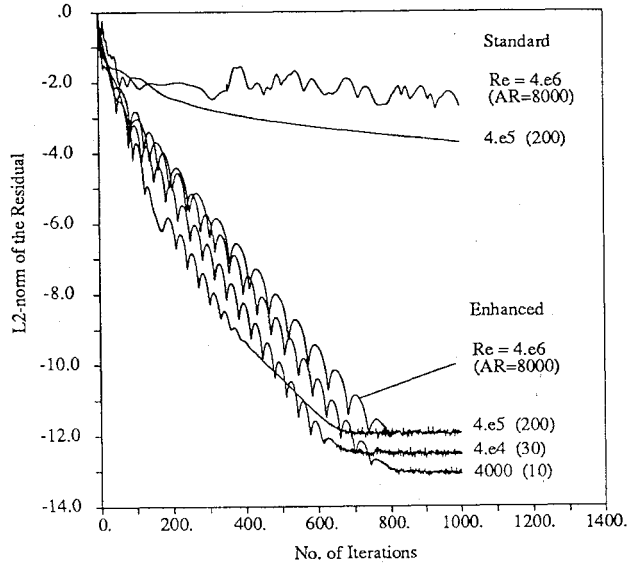

Fig. 11 Laminar boundary-layer solution.

the Blasius profile, whereas the turbulent profile (Fig. 12) is plotted against the law of the wall and the log-law profiles. In both instances, there is good agreement between the numerical predictions and theory, thereby confirming that the improved algorithm converges to the correct solution.

Converging-Diverging Nozzle

The final case that we examine is high-Reynolds-number turbulent flow through a converging-diverging nozzle with cooled walls. The grid geometry (141 × 121) and flowfield solution are shown in Fig. 13. The incoming gas is at a stagnation temperature of 3500 K, whereas the wall is maintained at 700 K. Of particular interest, for this case, is the accurate prediction of the heat flux to the nozzle wall. Because of the extremely thin boundary layer in the throat region, very strong grid stretching is necessary to maintain a minimum y^+ of about 1 along the wall. Accordingly, the corresponding maximum grid aspect ratio is 2×10^6.

The convergence results are shown in Fig. 14. With the enhanced algorithm, rapid convergence is obtained with machine zero being reached in less than 2000 iterations. With the standard algorithm, the convergence is fairly good for about four orders of magnitude reduction in the residual beyond which it becomes very poor. Examination of the residuals indicates that the initial portion corresponds to solution convergence in the central portion of the flowfield where

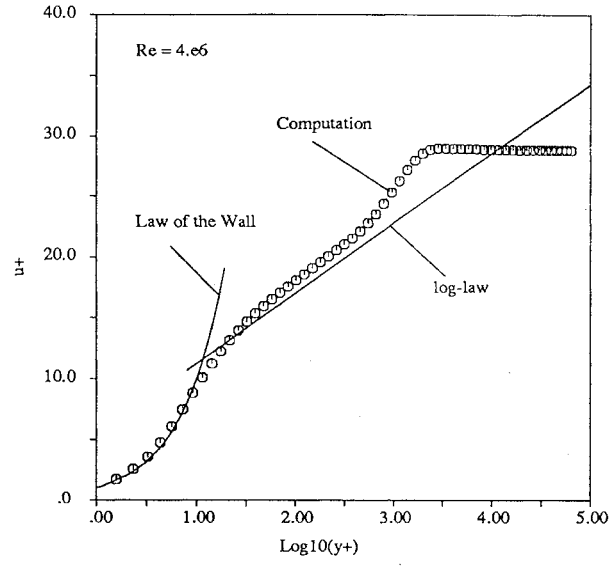

Fig. 12 Turbulent boundary-layer solution.

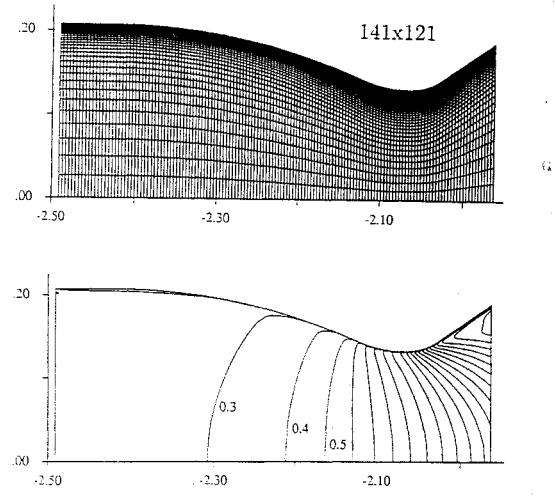

Fig. 13 Stretched grid and Mach contours for turbulent nozzle computation.

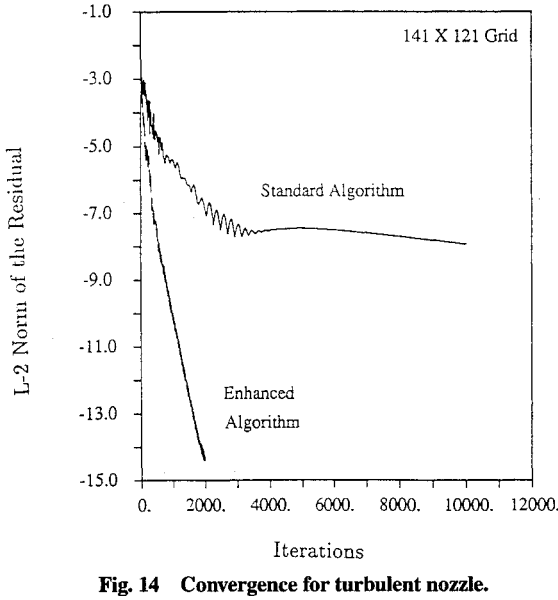

Fig. 14 Convergence for turbulent nozzle.

the grids are more or less regular, whereas the latter portion is due to poor convergence in the high-aspect-ratio near-wall region. This is also readily apparent by observing the temporal convergence of the wall heat flux shown in Fig. 15 for both the standard and enhanced algorithms.

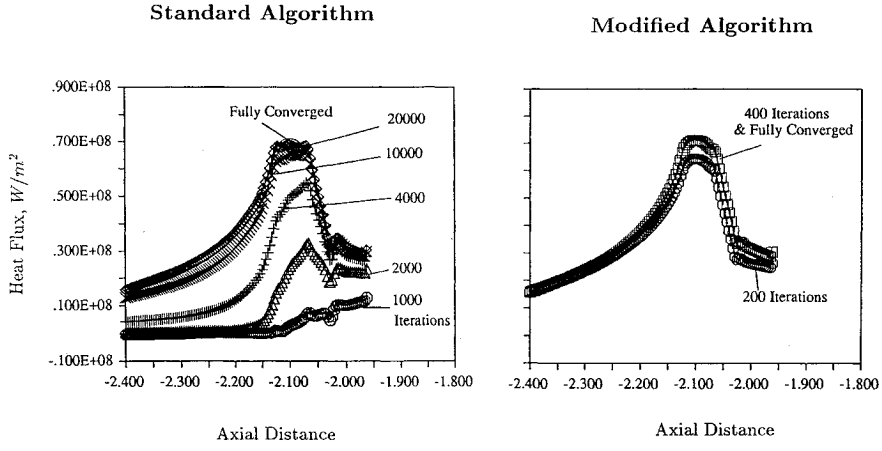

Fig. 15 Temporal convergence of nozzle wall heat flux.

The results in Fig. 15 for the standard algorithm without aspect ratio control indicate that after a three order-of-magnitude reduction in the residual (after 2000 iterations), the wall heat flux is far from converged. Converging the flowfield an additional order of magnitude (after 4000 iterations) causes the wall heat flux to change by almost a factor of 2. It requires roughly 20,000 iterations (about six orders of magnitude convergence) for the heat flux to be approximately the same as the fully converged result. On the other hand, with the enhanced algorithm, the wall heat flux converges at the same rate as the overall flowfield and a three order-of-magnitude reduction in residual (less than 400 iterations) is sufficient to give wall heat flux to engineering accuracy. Thus, the convergence enhancement methods discussed in this paper can significantly impact realistic flow computations.

Summary

The effects of high-grid-aspect ratios are well known to impact convergence adversely for all types of computational algorithms. In the present paper, we have concentrated on identifying the degree of convergence deterioration in ADI schemes as grid aspect ratio increases and on deriving methods for circumventing this problem. Our procedure has followed a logical step-by-step approach. The initial step has been to use vector stability analyses of the Euler and the Navier-Stokes equations to identify those locations in the wave number domain that cause convergence deterioration as aspect ratio is increased. The Euler results demonstrate that approximate factorization errors are not significant until the magnitude of the product of CFL_x and CFL_y is large relative to the maximum CFL number. At $AR = 1$, this occurs for CFL between 1 and 10. For larger aspect ratios, it does not happen until the $CFL_{\max}$ is of the order of the aspect ratio or the $CFL_{\min}$ is between 1 and 10. This suggests that if the local time step is defined based on the $CFL_{\min}$ (rather than the $CFL_{\max}$, as is conventionally done), the ADI scheme will provide efficient convergence at all aspect ratios.

Companion stability results for the Navier-Stokes equations show that the most offending approximate factorization error is the product of CFL_x and VNN_y. Because of this inviscid-viscous approximate factorization error, it becomes necessary in Navier-Stokes solutions to base the local time step on the value of the minimum CFL and the maximum VNN. The use of viscous preconditioning allows both of these time scales to be optimized simultaneously.

Extensive computational experiments starting first with simple flows and then going to realistic problems demonstrate that the combination of properly defined local time step and preconditioning gives uniform convergence for grid aspect ratios from one to one million. The convergence results, however, are often sensitive to the boundary conditions. The various very large CFL's used in the calculations make it imperative that properly formulated MOC procedures be applied at the boundaries.

Inspection of the explicit central difference algorithms indicates that the same method fails for explicit schemes because of the strong upper limit on CFL that accompanies these methods. The more forgiving implicit schemes allow one CFL (CFL_x or CFL_y) to be raised far above its normal optimum value without detriment, and this is why the method is successful for implicit methods. Extensions to three-dimensional problems and upwind algorithms is currently under way.

Acknowledgments

This work was sponsored by the NASA Marshall Space Flight Center under Contract NAS8-38861 and the NASA Propulsion Engineering Research Center at the Pennsylvania State University under NASA Contract NAGW-1356.

References

[1]Turkel, E., "Review of Preconditioning Methods for Fluid Dynamics," NASA CR 189712; see also Inst. for Computer Applications in Science and Engineering, ICASE Rep. 92-47, Hampton, VA.

[2]Choi, Y.-H., and Merkle, C. L., "The Application of Preconditioning to Viscous Flows," *Journal of Computational Physics*, Vol. 105, No. 2, 1993, pp. 207–223.

[3]Venkateswaran, S., Weiss, J. M., Merkle, C. L., and Choi, Y.-H., "Propulsion-Related Flowfields Using the Preconditioned Navier-Stokes Equations," AIAA Paper 92-3437, July 1992.

[4]Shuen, J.-S., Chen, K.-H., and Choi, Y.-H., "A Coupled Implicit Method for Chemical Non-Equilibrium Flows at All Speeds," *Journal of Computational Physics*, Vol. 106, 1993, pp. 306.

[5]van Leer, B., Lee, W. T., and Roe, P. L., "Characteristic Time-Stepping or Local Preconditioning of the Euler Equations," AIAA Paper 91-1552 June 1991.

[6]Godfrey, A. G., Walters, R. W., and van Leer, B., "Preconditioning for the Navier-Stokes Equations," AIAA Paper 93-0535, Jan. 1993.

[7]Briley, W. R., Govindan, T. R., and McDonald, H., "Efficient Navier-Stokes Flow Prediction Algorithms," NASA CR NAS8-37340, June 1990.

[8]Martinelli, L., "Calculation of Viscous Flows with a Multi-Grid Method," Ph.D. Dissertation, Dept. of Mechanical and Aerospace Engineering, Princeton Univ., Princeton, NJ, Oct. 1987.

[9]van Leer, B., private communication.

[10]Douglas, J., and Gunn, J. E., "A General Formulation of Alternating Direction Method—Part I—Parabolic and Hyperbolic Problem," *Numerische Mathematik*, Vol. 82, 1964, pp. 428–453.

[11]Briley, W. R., McDonald, H., and Shamroth, S. J., "A Low Mach Number Euler Formulation and Application to Time-Iterative LBI Schemes," *AIAA Journal*, Vol. 21, pp. 1467–1469.

[12]Warming, R. F., and Beam, R. M., "On the Construction and Application of Implicit Factored Schemes for Conservation Law," *SIAM-AMS Proceedings*, Vol. 11, 1978, pp. 85–129.

[13]Rai, M. M., and Chaussee, D. S., "New Implicit Boundary Procedures: Theory and Application," *AIAA Journal*, Vol. 22, No. 8, 1984, pp. 1094–1100.

[14]Chakravarthy, S. R., "Euler Equations—Implicit Schemes and Boundary Conditions," *AIAA Journal*, Vol. 21, No. 5, 1983, pp. 669–706.

[15]Yu, S.-T., Hultgren, L. S., and Liu, N.-S., "Direct Calculations of Waves in Fluid Flows Using High-Order Compact Difference Scheme," AIAA Paper 93-0148, Jan. 1993.

[16]Baldwin, B. S., and Lomax, H., "Thin Layer Approximation and Algebraic Model for Separated Turbulent Flows," AIAA Paper 78-257, Jan. 1978.